

## LA-UR-20-27793

Approved for public release; distribution is unlimited.

Title: Investigating bubble pressures in irradiated UO<sub>2</sub> for understanding fragmentation of high burnup structure

Author(s): Cooper, Michael William Donald  
Matthews, Christopher  
Andersson, Anders David Ragnar

Intended for: Report

Issued: 2021-03-24 (rev.1)

---

**Disclaimer:**

Los Alamos National Laboratory, an affirmative action/equal opportunity employer, is operated by Triad National Security, LLC for the National Nuclear Security Administration of U.S. Department of Energy under contract 89233218CNA000001. By approving this article, the publisher recognizes that the U.S. Government retains nonexclusive, royalty-free license to publish or reproduce the published form of this contribution, or to allow others to do so, for U.S. Government purposes. Los Alamos National Laboratory requests that the publisher identify this article as work performed under the auspices of the U.S. Department of Energy. Los Alamos National Laboratory strongly supports academic freedom and a researcher's right to publish; as an institution, however, the Laboratory does not endorse the viewpoint of a publication or guarantee its technical correctness.



# **Investigating bubble pressures in irradiated $\text{UO}_2$ for understanding fragmentation of high burnup structure**

M. W. D. Cooper, C. Matthews, and D. A. Andersson

*Materials Science and Technology Division, Los Alamos National Laboratory*

September 30, 2020

# Executive Summary

This report summarized work carried out to investigate mechanisms relevant to fragmentation of high burnup  $\text{UO}_2$  fuel. High pressure bubbles that form in high burnup structure are thought to be responsible for fragmentation and pulverization, when exposed to a temperature ramp during a transient. The over-pressurization of the bubbles during normal operation is a pre-requisite for this mechanism to occur. Therefore, in this work we investigate the role of interstitials, produced through irradiation, in over-pressurizing the bubbles by using a combined molecular dynamics (MD) and cluster dynamics approach. Firstly, the energies for the annihilation of interstitials and vacancies at bubbles have been determined from MD as a function of bubble pressure. Secondly, these reaction energies have been implemented in the cluster dynamics code Centipede to determine the steady-state defect concentrations and bubble pressure under irradiation. It was found that there is a transition from low pressure bubbles, at high temperature, to high pressure bubbles, at low temperatures. This indicates the formation of over-pressurized bubbles in the low temperature periphery of the pellet, where high burnup structure forms. This result supports the hypothesis that over-pressurized bubbles form during steady-state operation and can then contribute to fragmentation during a transient. Future work will examine the influence of bubble pressure on Xe diffusion and study the impact of other sinks (e.g. grain boundaries and dislocations) that are relevant to high burnup structure. Ultimately, the goal is to provide predictions of the bubble pressure as a function of burnup that can be used to derive a more mechanistic fragmentation threshold for use in BISON.

# Contents

<b>1</b>	<b>Introduction</b>	<b>1</b>
<b>2</b>	<b>Methods</b>	<b>3</b>
2.1	Potential model . . . . .	3
2.2	Bubble MD calculations . . . . .	4
2.3	Cluster dynamics . . . . .	4
<b>3</b>	<b>Results and Discussion</b>	<b>6</b>
3.1	Development of bubble energetics data from MD . . . . .	6
3.1.1	Unmodified sinks . . . . .	6
3.1.2	Void . . . . .	7
3.1.3	Bubbles . . . . .	8
3.1.4	Non-stoichiometric defects . . . . .	11
3.2	Cluster dynamics simulations . . . . .	13
3.2.1	Unmodified sinks . . . . .	13
3.2.2	Fixed bubble pressure . . . . .	13
3.2.3	Variable bubble pressure . . . . .	14
<b>4</b>	<b>Conclusions</b>	<b>18</b>

## List of Figures

3.1	A schematic of a damage event, which generates Frenkel pairs, and the subsequent diffusion of the interstitial to a bubble. The bubble volume reduces slightly, compressing the gas within it. . . . .	6
3.2	The change in the supercell energy containing a void, with respect to the perfect supercell, as a function of the number $\text{UO}_2$ formula units removed to create the void ( $N_{SD}$ ). . . . .	8
3.3	The energy per atom required to incorporate $N_{Xe}$ Xe atoms, for three different bubble sizes. The data is plotted as a function of $N_{Xe}$ divided by the number of $\text{UO}_2$ formula units removed to create the void ( $N_{SD}$ ). This fraction is analogous to the pressure. A polynomial fit to this data that was used to determine reaction energies is shown by the black line. . . . .	9
3.4	The reaction energies for the interaction of interstitial and vacancy clusters with a bubble, as a function of $\frac{N_{Xe}}{N_{SD}}$ . . . . .	11
3.5	(a) The defect concentrations and (b) the defect diffusivities predicted by cluster dynamics simulations of $\text{UO}_2$ using the standard sink reactions in Centipede. . . . .	13
3.6	The defect concentrations predicted by cluster dynamics simulations of $\text{UO}_2$ , where the sink reactions in Centipede have been modified for different constant bubble pressures according to Eqs. (3.31) and (3.32). The simulations were run at (a) 800 K and (b) 2200 K. (a) and (b) show a subset of the defects considered by Centipede. . . . .	14
3.7	(a) The defect concentrations and (b) the defect diffusivities predicted by cluster dynamics simulations of $\text{UO}_2$ , where (c) the steady-state bubble pressure is also solved for. . . . .	16
3.8	The steady-state bubble pressure, represented by $\frac{N_{Xe}}{N_{SD}}$ , determined using different initial values of $\frac{N_{Xe}}{N_{SD}}$ . . . . .	17

# 1 Introduction

UO<sub>2</sub> has been the dominant nuclear fuel material for commercial light water reactors (LWRs) since their conception. One of the current objectives of LWR operators is to extend the burnup of UO<sub>2</sub> fuel. During burnup, the fuel experiences extreme irradiation damage and accumulation of fission products, resulting in significant microstructural changes. In the periphery of the pellet, where low temperatures limit annealing of irradiation induced defects and prevent the release of insoluble fission products, UO<sub>2</sub> undergoes a restructuring forming the so-called high burnup structure (HBS). HBS is characterized by a reduction in grain size and the formation of micron-sized bubbles [1–6]. The formation of HBS is associated with high burnups in the cooler periphery of the pellet [1, 7]. The reduction of grain size is due to the formation of sub-grains. Lozano et al. [8] identified two types of sub-grain formation: i) 0.8  $\mu\text{m}$  polyhedral grains and ii) 0.1  $\mu\text{m}$  round grains associated with pores or large bubbles. Coarsening of fission gas bubbles to micron-sizes is typical of HBS and has been widely observed [2–5, 9]. However, in some (but not all) studies evidence has also been found that the sub-grain boundaries are decorated with nm-sized bubbles [1, 5]. Sonoda et al. [5] used TEM to observe bubbles at sub-grain boundaries in the range of 3.5–8 nm in size.

The formation of HBS is important for nuclear fuel performance as the material properties are dependent on the microstructural changes. For example, a recovery in the thermal conductivity of the fuel is associated with HBS formation [10] and has been attributed to a decrease in Xe concentrations in the UO<sub>2</sub> lattice [11, 12]. Another critical impact of HBS on fuel behavior, and by far the most important for extended burnups, is the fragmentation and pulverization of the HBS regions of the pellet during transient conditions [13]. Pulverization is defined as disintegration of the fuel to mostly micron-size particles with none larger than 1 mm, whereas fragmentation results in particles of  $>1$  mm. Turnbull et al. [13] presented a review of experiments carried out under the NFIR program, showing that pulverization typically resulted in particles of 20–200  $\mu\text{m}$  in size. In that work, thresholds were defined for the local burnup (71 MWd/kgU) and peak transient temperature (918 K) required to cause pulverization. The burnup threshold essentially relates to the onset of formation of HBS. The temperature threshold, required to observe pulverization during a transient, is related to the fracture mechanism itself. It has been suggested by Turnbull et al. [13] that the expansion of over-pressurized bubbles during the temperature ramp cause fragmentation/pulverization.

Atomic scale simulations are a useful tool to investigate the underlying mechanisms that govern fission gas behavior and its potential role in fuel fragmentation. Much of the extensive atomic scale work that has been undertaken on UO<sub>2</sub> has focused on intrinsic and irradiation-enhanced fission gas diffusion [14–22]. Other issues around fission gas behavior have included molecular dynamics simulations of bubble formation [23, 24], resolution from bubbles under irradiation [25–27], and enhanced Xe diffusion and nucleation of bubbles at dislocations [28]. Matthews et al. [29, 30] have developed a cluster dynamics framework that accurately captures

irradiation-enhanced U and Xe diffusion in  $\text{UO}_2$ . In order to reproduce experimentally observed behavior a wide range of defect clusters had to be considered. In particular, the diffusion of mobile bound anti-Schottky trios had to be included. The irradiation-enhanced diffusion of these defects have the potential to play a significant role in the over-pressurization of bubble in the periphery of the pellet, where HBS forms.

In this work, we employed MD simulations to derive reaction energies for the interaction of interstitials and vacancies with bubbles. These energies were then used to modify the sink reaction energies within the cluster dynamics code Centipede to account for the bubble pressure. By solving simultaneously for the defect concentrations and bubble pressure under irradiation, the possibility of the over-pressurization of bubbles in the periphery of the pellet is analyzed.



## 2 Methods

### 2.1 Potential model

MD simulations, employing a set of interatomic potentials for  $\text{UO}_2$  derived previously by Cooper, Rushton, and Grimes (CRG) [31] were carried out using the Large-scale Atomic/Molecular Massively Parallel Simulator (LAMMPS) [32]. In this model the potential energy,  $E_i$ , of an atom  $i$  with respect to all other atoms has two components - i) a pair potential description of each system and ii) a many-body embedded atom method (EAM) contribution, using the model of Daw and Baskes [33]:

$$E_i = \frac{1}{2} \sum_j \phi_{\alpha\beta}(r_{ij}) - G_\alpha \left( \sum_j \sigma_\beta(r_{ij}) \right)^{\frac{1}{2}} \quad (2.1)$$

where the pairwise interaction between two atoms  $i$  and  $j$ , separated by  $r_{ij}$ , is given by  $\phi_{\alpha\beta}(r_{ij})$  (equation 2.2) and has both long range electrostatic,  $\phi_C(r_{ij})$  (equation 2.3), and short range contributions. The former were calculated using the Ewald method [34] with the Particle-Particle Particle-Mesh (PPPM) implementation of the method being adopted in order to improve computational efficiency [35]. The short range contributions are described using Morse,  $\phi_M(r_{ij})$  (equation 2.4), and Buckingham,  $\phi_B(r_{ij})$  (equation 2.5), potential forms [36, 37].  $\alpha$  and  $\beta$  are used to label the species of atom  $i$  and atom  $j$ , respectively.

$$\phi_{\alpha\beta}(r_{ij}) = \phi_C(r_{ij}) + \phi_B(r_{ij}) + \phi_M(r_{ij}) \quad (2.2)$$

$$\phi_C(r_{ij}) = \frac{q_\alpha q_\beta}{4\pi\epsilon_0 r_{ij}} \quad (2.3)$$

$$\phi_M(r_{ij}) = D_{\alpha\beta} [\exp(-2\gamma_{\alpha\beta}(r_{ij} - r_{\alpha\beta}^0)) - 2\exp(-\gamma_{\alpha\beta}(r_{ij} - r_{\alpha\beta}^0))] \quad (2.4)$$

$$\phi_B(r_{ij}) = A_{\alpha\beta} \exp\left(\frac{-r_{ij}}{\rho_{\alpha\beta}}\right) - \frac{C_{\alpha\beta}}{r_{ij}^6} \quad (2.5)$$

where  $A_{\alpha\beta}$ ,  $\rho_{\alpha\beta}$ ,  $C_{\alpha\beta}$ ,  $D_{\alpha\beta}$ ,  $\gamma_{\alpha\beta}$  and  $r_{\alpha\beta}^0$  are empirical parameters that describe the pair interactions between atom  $i$  and atom  $j$ . Partial charges ( $q_\alpha$ ) are used that are proportional to the formal charges ( $Q_\alpha$ ), such that  $q_\alpha = \xi Q_\alpha$ , where the ionicity,  $\xi$ , is 0.5552 for all ions.

The second term in equation 2.1 uses the EAM to introduce a many-body perturbation to the pairwise interactions. The many-body dependence is achieved by summing a set of pairwise interactions,  $\sum_j \sigma_\beta(r_{ij})$ , and passing this through a non-linear embedding function:  $\sigma_\beta(r_{ij})$  is inversely proportional to the 8<sup>th</sup> power of the inter-ionic separation (equation 2.6) and a square root embedding function is used (equation 2.1), where  $n_\beta$  and  $G_\alpha$  are the respective constants of

proportionality. The derivation of the parameters and a description of the functional terms used in the EAM component are given in references [31].

$$\sigma_{\beta}(r_{ij}) = \left( \frac{n_{\beta}}{r_{ij}^8} \right) \frac{1}{2} (1 + \operatorname{erf}(20(r - 1.5))) \quad (2.6)$$

In order to prevent unrealistic forces occurring at short separations, a short range cut-off using an error function is applied at 1.5 Å that reduces the EAM component gradually. This ensures that there is no discontinuity in the interatomic energy, which would arise from an abrupt cut-off.

Xe-U and Xe-O interactions are taken from the work of Cooper et al. [38] and Xe-Xe interactions are from Tang and Toennies [39].

## 2.2 Bubble MD calculations

MD simulations, using the CRG potential, have been employed to generate reaction energies for the interaction of interstitials and vacancies with bubbles as a function of bubble pressure. Spherical voids of different sizes (from 2 nm to 5 nm) were created in a supercell made up of a  $20 \times 20 \times 20$  extension of the fluorite  $\text{UO}_2$  unit cell. When creating the voids, often U and O atoms were removed at a non-stoichiometric ratio. Therefore, to preserve the stoichiometry of the system O atoms were added or removed from the surface of the void. To enable the O atoms to relocate to a more favorable configuration the system was annealed at 1000 K and then cooled to 100 K before energy minimization at zero pressure. Xe atoms were then placed into the void in varying numbers to create bubbles of varying pressure. The Xe atoms were also annealed (while keeping the U and O atoms fixed) to 1000 K before cooling to 100 K. Finally, energy minimization on all atoms was carried out at constant volume to determine the 0 K energy of the bubble. The energy of the bubble as a function of bubble size and number of gas atoms has been used to determine the reaction energies for interstitials and vacancies interacting with bubbles.

## 2.3 Cluster dynamics

The details of the Centipede code are given in [29], however we repeat some of those details here to provide context to the modifications made in the results section. Currently, Centipede uses sinks based on fission gas bubbles that are treated as ideal reservoirs. This means their nature is not altered by the reaction with interstitials or vacancies, as such:



where standard Kröger-Vink notation is used [40], but with charges excluded for simplicity. The superscript for the energy denotes the specific type of reaction the energy represents, in this case a standard sink reaction. Given that the energy of the sink is unchanged by the reaction, the

energy of the reaction to go forwards is the negative of the vacancy and interstitial formation energies,  $G_{V_U}^f$  and  $G_{U_i}^f$ :

$$G_{V_U}^{sink} = -G_{V_U}^f \quad (2.9)$$

$$G_{U_i}^{sink} = -G_{U_i}^f \quad (2.10)$$

The total contribution to the free energy of the system from vacancies and interstitials is given by:

$$G_{V_U} = [V_U]G_{V_U}^f + [V_U]k_B T \ln([V_U]) \quad (2.11)$$

$$G_{U_i} = [U_i]G_{U_i}^f + [U_i]k_B T \ln([U_i]) \quad (2.12)$$

where  $[V_U]$  and  $[U_i]$  are the concentrations of vacancies and interstitials, respectively. Although the formation energy of perfect lattice sites,  $U_U$  and  $V_i$ , are zero, their configurational entropy must still be included in the total free energy, as such:

$$G_{U_U} = [U_U]k_B T \ln([U_U]) \quad (2.13)$$

$$G_{V_i} = [V_i]k_B T \ln([V_i]) \quad (2.14)$$

where  $[U_U]$  and  $[V_i]$  are dependent on the concentration of all defects in the system and do not need to be solved for explicitly.

The driving force,  $f$ , for the sink reactions, Eqs. (2.7) and (2.8), are given by the derivative of the total free energy of the system,  $G$ , due to the change in concentration of the above defects:

$$f = \frac{\partial G}{\partial [U_U]} - \frac{\partial G}{\partial [V_U]} = -G_{V_U}^f - k_B T \ln([V_U]) + k_B T \ln([U_U]) \quad (2.15)$$

$$f = \frac{\partial G}{\partial [V_i]} - \frac{\partial G}{\partial [U_i]} = -G_{U_i}^f - k_B T \ln([U_i]) + k_B T \ln([V_i]) \quad (2.16)$$

As  $f \rightarrow 0$  the solution for the thermal equilibrium defect concentrations is obtained (and in the point defect limit specifically the Arrhenius function). Hence, the sinks currently used in Centipede always try to return the system to equilibrium. This is further demonstrated by the equation for the sink reaction rate for defect  $A$ ,  $\frac{d[A]}{dt}$ , whereby as  $f \rightarrow 0$  the  $\frac{d[A]}{dt} \rightarrow 0$ :

$$\frac{d[A]}{dt} = \begin{cases} -\frac{k_s^2}{\Omega} D_A [A] [sink] \left[ 1 - \exp\left(\frac{f}{k_B T}\right) \right], & \text{if } f < 0, \\ \frac{k_s^2}{\Omega} D_A [sink] \left[ \exp\left(\frac{-f}{k_B T}\right) - 1 \right], & \text{otherwise} \end{cases} \quad (2.17)$$

where  $k_s^2$  is the reduced reaction constant,  $\Omega$  is the atomic volume, and  $D_A$  is the diffusivity of defect  $A$ . By treating the sinks as bubbles  $k_s^2[sink]$  can be rewritten as [29]:

$$k_s^2[sink] = 4\pi\Omega\langle R_{bub}C_{bub} \rangle = 0.586 \text{ nm} \quad (2.18)$$

where  $\langle R_{bub}C_{bub} \rangle$  has been shown to be fairly constant across different samples based on Refs. [41, 42]. In this work, modifications to the driving force have been made to enable Centipede to solve for the bubble pressure and to account for this pressure in the sink reaction rates for interstitials and vacancies.

## 3 Results and Discussion

### 3.1 Development of bubble energetics data from MD

The objective of this work is to modify the sink reaction energies in Centipede to account for bubble pressure. By implementing this in Centipede the bubble pressure will, in turn, be updated according to the reaction rates for interstitials (increasing pressure) and vacancies (decreasing pressure) being annihilated at bubbles.

As shown in the work of Matthews et al. [29], the contribution of U interstitials to diffusivity at low temperature is far greater than that of U vacancies. It is expected, therefore, that there will be a greater arrival rate for interstitials at bubbles than vacancies. Each interstitial that arrives at a bubble will shrink it slightly. Figure 3.1 shows a schematic representation of the process we are attempting to capture, whereby an interstitial produced by irradiation is captured by a bubble. The bubble, in response, decreases its volume and compresses the gas within the bubble. The reaction energy for the interstitial (or vacancy) to annihilate at the bubble will depend on the bubble pressure, affecting the reaction rate via a new pressure dependent Eq. (2.17). The net flow of vacancies and interstitials will control the change in the bubble pressure.

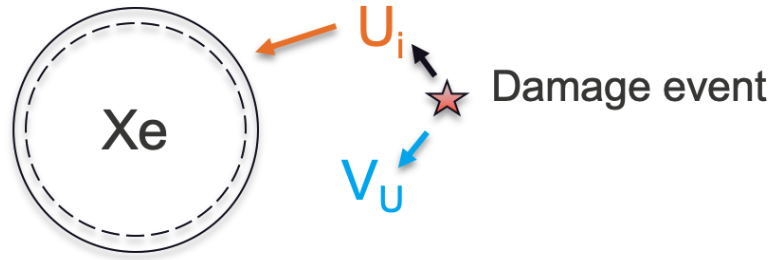


Figure 3.1: A schematic of a damage event, which generates Frenkel pairs, and the subsequent diffusion of the interstitial to a bubble. The bubble volume reduces slightly, compressing the gas within it.

#### 3.1.1 Unmodified sinks

In order to modify Eq. (2.17) to account for the bubble pressure, we must first derive energies for the appropriate reactions from MD. Given that the growth of a bubble requires the stoichiometric addition or removal of  $\text{UO}_2$  formula units we have first chosen to deal only with stoichiometric defect clusters, and will discuss non-stoichiometric defects later. The ideal sink reactions for non-stoichiometric point defects ( $V_U$  and  $U_i$ ) given by Eqs. (2.7) and (2.8), can be rewritten as

follows for stoichiometric bound Schottky,  $\{V_U : 2V_O\}$ , or anti-Schottky trios,  $\{U_i : 2O_i\}$ :



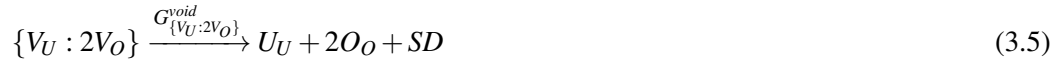
where the *sink* species from Eqs. (2.7) and (2.8) has been replaced by a bulk  $UO_2$  formula unit (equivalent sourcing one U atom and two O atoms from an infinite reservoir that has the same chemical potential as the rest of system). The energies of Eq. (3.1) and Eq. (3.2) are exactly equal to the negative of the formation energy of  $\{V_U : 2V_O\}_{bulk}$  and  $\{U_i : 2O_i\}_{bulk}$ , such that

$$G_{\{V_U : 2V_O\}}^{sink} = -G_{\{V_U : 2V_O\}}^f \quad (3.3)$$

$$G_{\{U_i : 2O_i\}}^{sink} = -G_{\{U_i : 2O_i\}}^f \quad (3.4)$$

### 3.1.2 Void

Before considering a bubble, let us first consider the defects reacting with a void. A void is created by the removal of  $UO_2$  formula units. Here we refer to the formula units removed to make a void as SD (due to their similarity to a **S**chottky **d**efect), such that a void is made up of  $N_{SD}$  SDs. Rather than taking or adding  $UO_2$  formula units from the bulk lattice, the reactions increase or decrease  $N_{SD}$ , as such:



The corresponding reaction energies are:

$$G_{\{V_U : 2V_O\}}^{void} = G_{\{V_U : 2V_O\}}^{sink} + E_{UO_2} + \frac{dE_{void}}{dN_{SD}} \quad (3.7)$$

$$G_{\{U_i : 2O_i\}}^{void} = G_{\{U_i : 2O_i\}}^{sink} - E_{UO_2} - \frac{dE_{void}}{dN_{SD}} \quad (3.8)$$

where  $E_{UO_2}$  is the lattice energy per  $UO_2$  formula unit, and  $\frac{dE_{void}}{dN_{SD}}$  is energy to change the number of SDs that make up the void. Therefore,  $E_{UO_2}$  and  $\frac{dE_{void}}{dN_{SD}}$  combined are a modification to the traditional sink reaction energy that accounts for interactions with a void.

Both  $E_{UO_2}$  and  $\frac{dE_{void}}{dN_{SD}}$  can be derived from MD calculations. Following the procedure outlined in Section 2.2, voids of various size ( $87 < N_{SD} < 1553$ ) were generated, annealed, then energy minimized. The energy of the void,  $E_{void}$ , is defined as the energy of the supercell containing the void minus the energy of the perfect supercell. Figure 3.2 shows  $E_{void}$  as a function of  $N_{SD}$ .

The following equation was fitted to the data in Fig. 3.2:

$$E_{void} = aN_{SD} + bN_{SD}^{2/3} \quad (3.9)$$

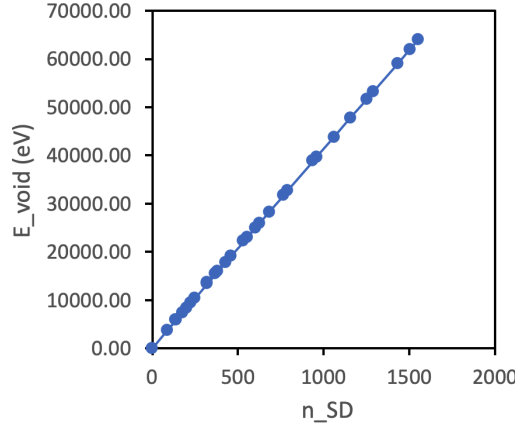


Figure 3.2: The change in the supercell energy containing a void, with respect to the perfect supercell, as a function of the number  $\text{UO}_2$  formula units removed to create the void ( $N_{SD}$ ).

where  $a = 40.67$  eV and  $b = 6.51$  eV. Physically  $a$  represents the energy to remove bulk  $\text{UO}_2$  formula units and  $b$  is related to the creation of the void surface. By calculating the energy of the perfect  $\text{UO}_2$  lattice it was confirmed that  $a = -E_{\text{UO}_2}$ . Therefore, the derivative  $\frac{dE_{\text{void}}}{dN_{SD}}$  is given by:

$$\frac{dE_{\text{void}}}{dN_{SD}} = -E_{\text{UO}_2} + \frac{2}{3}bN_{SD}^{-1/3} \quad (3.10)$$

The second term is relatively small compared to the first, so to simplify implementation in Centipede,  $\frac{dE_{\text{void}}}{dN_{SD}}$  is assumed to be equal to  $-E_{\text{UO}_2}$ . Therefore, Eqs. (3.7) and (3.8) can be simplified to show they are equivalent to the traditional sink reaction energies:

$$G_{\{V_U:2V_O\}}^{\text{void}} = G_{\{V_U:2V_O\}}^{\text{sink}} = -G_{\{V_U:2V_O\}}^f \quad (3.11)$$

$$G_{\{U_i:2O_i\}}^{\text{void}} = G_{\{U_i:2O_i\}}^{\text{sink}} = -G_{\{U_i:2O_i\}}^f \quad (3.12)$$

### 3.1.3 Bubbles

Having shown that it is sufficient to consider the reactions for interstitials and vacancies with a void as equivalent to the traditional sink reactions already included in Centipede, we now account for the reactions with a bubble:



where SD is now located at a bubble with a certain pressure rather than at a void as discussed earlier. In order to account for this, an expression must be derived for the change in the energy of the bubbles due to the addition or removal of SDs,  $\frac{dE_{\text{bubble}}}{dN_{SD}}$ .

Following the procedure outlined in Section 2.2, Xe atoms were incorporated into spherical voids with diameters of 3 nm ( $N_{SD} = 369$ ), 4 nm ( $N_{SD} = 491$ ), and 5 nm ( $N_{SD} = 1553$ ). The number of Xe ( $N_{Xe}$ ) incorporated into the voids was in the range  $0 < \frac{N_{Xe}}{N_{SD}} < 4$ . Due to the convenience of treating reaction energies in terms of the number of species involved in the reaction,  $\frac{N_{Xe}}{N_{SD}}$  is used as an alternative to the bubble pressure. The greater  $\frac{N_{Xe}}{N_{SD}}$  is, the greater the bubble pressure.

For all bubbles the gas was annealed, while keeping the U and O atoms frozen, to allow it to reconfigure. Subsequently, all atoms were allowed to relax during energy minimization to determine the system energy. The change in the energy of the system, with respect to the void, divided by  $N_{Xe}$  (average Xe incorporation energy) is shown in Fig. 3.3, as a function of  $\frac{N_{Xe}}{N_{SD}}$ . As expected, for low  $\frac{N_{Xe}}{N_{SD}}$  there is a negligible incorporation energy given that the gas atoms take up a much small volume that the space provided by the void. As  $\frac{N_{Xe}}{N_{SD}}$  increases above 1 the incorporation energy for the gas increases significantly, demonstrating that it get progressively more difficult to incorporate gas into the high pressure bubbles.

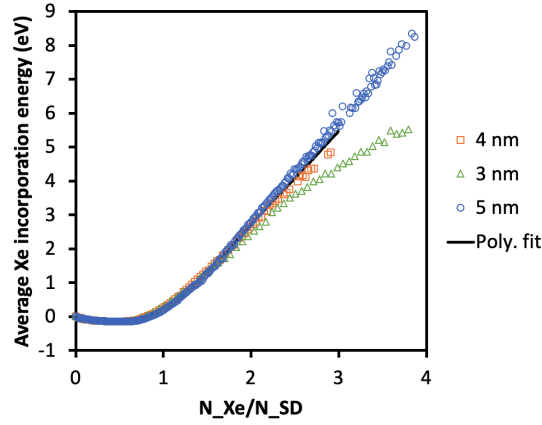


Figure 3.3: The energy per atom required to incorporate  $N_{Xe}$  Xe atoms, for three different bubble sizes. The data is plotted as a function of  $N_{Xe}$  divided by the number of  $\text{UO}_2$  formula units removed to create the void ( $N_{SD}$ ). This fraction is analogous to the pressure. A polynomial fit to this data that was used to determine reaction energies is shown by the black line.

Importantly for developing data that can be readily implemented in Centipede, it can be seen that in the range  $0 < \frac{N_{Xe}}{N_{SD}} < 2$  all three bubble sizes show the same trend.  $\frac{N_{Xe}}{N_{SD}} > 2$  represents very high bubble pressures that are unlikely to ever form. Therefore, we have fitted a single polynomial to capture the behavior of all bubble sizes:

$$\begin{aligned} \frac{E_{\text{bubble}} - E_{\text{void}}}{N_{Xe}} = & A \left( \frac{N_{Xe}}{N_{SD}} \right)^8 + B \left( \frac{N_{Xe}}{N_{SD}} \right)^7 + C \left( \frac{N_{Xe}}{N_{SD}} \right)^6 \\ & + D \left( \frac{N_{Xe}}{N_{SD}} \right)^5 + E \left( \frac{N_{Xe}}{N_{SD}} \right)^4 + F \left( \frac{N_{Xe}}{N_{SD}} \right)^3 + G \left( \frac{N_{Xe}}{N_{SD}} \right)^2 + H \left( \frac{N_{Xe}}{N_{SD}} \right) \end{aligned} \quad (3.15)$$

$$A = 0.02210 \text{ eV}$$

$$B = -0.3282 \text{ eV}$$

$$\begin{aligned}
C &= 1.950 \text{ eV} \\
D &= -5.858 \text{ eV} \\
E &= 9.189 \text{ eV} \\
F &= -7.091 \text{ eV} \\
G &= 3.372 \text{ eV} \\
H &= -1.033 \text{ eV}
\end{aligned}$$

By multiplying through by  $N_{Xe}$  then taking the derivative with respect to  $N_{SD}$ , we obtain:

$$\begin{aligned}
\frac{d(E_{bubble} - E_{void})}{dN_{SD}} &= -8A \left( \frac{N_{Xe}}{N_{SD}} \right)^9 - 7B \left( \frac{N_{Xe}}{N_{SD}} \right)^8 - 6C \left( \frac{N_{Xe}}{N_{SD}} \right)^7 \\
&\quad - 5D \left( \frac{N_{Xe}}{N_{SD}} \right)^4 - 4E \left( \frac{N_{Xe}}{N_{SD}} \right)^5 - 3F \left( \frac{N_{Xe}}{N_{SD}} \right)^4 - 2G \left( \frac{N_{Xe}}{N_{SD}} \right)^3 - H \left( \frac{N_{Xe}}{N_{SD}} \right)^2 \quad (3.16)
\end{aligned}$$

This expression can be used to modify the traditional sink reactions in Centipede as follows. Following the same logic as for the voids in Section 3.1.2, the reaction energies for Eqs. (3.13) and (3.14) are given by:

$$G_{\{V_U:2V_O\}}^{bubble} = G_{\{V_U:2V_O\}}^{sink} + E_{UO_2} + \frac{dE_{bubble}}{dN_{SD}} \quad (3.17)$$

$$G_{\{U_i:2O_i\}}^{bubble} = G_{\{U_i:2O_i\}}^{sink} - E_{UO_2} - \frac{dE_{bubble}}{dN_{SD}} \quad (3.18)$$

Given that  $\frac{dE_{bubble}}{dN_{SD}} = \frac{d(E_{bubble} - E_{void})}{dN_{SD}} + \frac{dE_{void}}{dN_{SD}}$  and, as was shown in Section 3.1.2,  $\frac{dE_{void}}{dN_{SD}} = -E_{UO_2}$ , this can be simplified to:

$$G_{\{V_U:2V_O\}}^{bubble} = G_{\{V_U:2V_O\}}^{sink} + \Delta E \quad (3.19)$$

$$G_{\{U_i:2O_i\}}^{bubble} = G_{\{U_i:2O_i\}}^{sink} - \Delta E \quad (3.20)$$

where:

$$\Delta E = \frac{d(E_{bubble} - E_{void})}{dN_{SD}} \quad (3.21)$$

Therefore, the driving force for the standard sink strengths in Centipede can be readily adjusted using Eq. (3.16). Given that 0 K calculations were used to derive Eq. (3.16) entropy terms have not been accounted for and should be considered in future work. Additionally, pressure release mechanisms have not been accounted for, such as dislocation punching, which may be activated at finite temperature.

To demonstrate the impact of Eq. (3.16) on Eqs. (3.19) and (3.20), Fig. 3.4 shows the sink reaction energies,  $G_{\{V_U:2V_O\}}^{bubble}$  and  $G_{\{U_i:2O_i\}}^{bubble}$ , as a function of  $\frac{N_{Xe}}{N_{SD}}$ . For  $\frac{N_{Xe}}{N_{SD}} = 0$ ,  $\Delta E = 0$  and the standard sink reaction energies are returned (i.e. the negative of the formation energies). Note that for this example the cluster formation energies are based on the CRG empirical potential and differ from the energies used in Centipede, which is based on DFT. As  $\frac{N_{Xe}}{N_{SD}}$  increases, the



reaction to annihilate a vacancy cluster becomes more exothermic. This is due to the release of Xe pressure, which lowers the bubble energy. Conversely, the energy released by annihilation of an interstitial cluster becomes less exothermic, as  $\frac{N_{Xe}}{N_{SD}}$  increases, due to the increased energy penalty of compressing the Xe atoms. Eventually, the reaction energy for the annihilation of the interstitial cluster reaches zero at  $\frac{N_{Xe}}{N_{SD}} \approx 2$ , above which the reaction become endothermic.

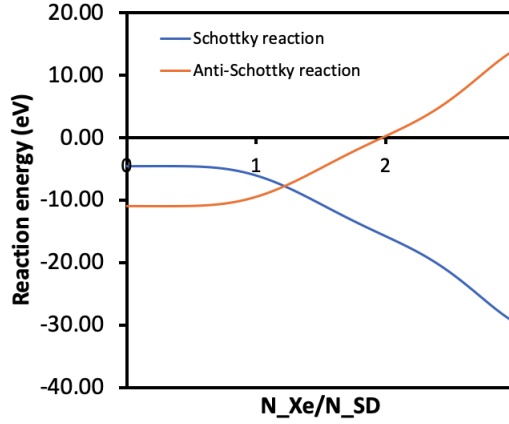


Figure 3.4: The reaction energies for the interaction of interstitial and vacancy clusters with a bubble, as a function of  $\frac{N_{Xe}}{N_{SD}}$ .

### 3.1.4 Non-stoichiometric defects

In Centipede,  $\{V_U : 2V_O\}$  and  $\{U_i : 2O_i\}$  are not solved for directly. Instead, they are linked to the point defects  $V_U$  and  $U_i$ , respectively, which are solved for as independent variables. The concentrations of  $\{V_U : 2V_O\}$  and  $\{U_i : 2O_i\}$  are coupled to the concentrations of  $V_U$  and  $U_i$  via thermodynamics that account for the energy to form and then bind to  $V_O$  and  $O_i$  defects. This treatment is based on the assumption that there is no kinetic hindrance for reactions involving oxygen defects due to their very high mobility, which allows them to remain at thermal equilibrium concentrations. Given that  $V_U$  and  $U_i$  are the solved variables, sink reactions must be defined that can be directly applied to them, rather than the stoichiometric clusters discussed so far.

If we start with  $V_U$ , we can consider a multistep process that leads to annihilation via a stoichiometric exchange with a bubble.

**Step 1** - Two oxygen vacancies must be created:



**Step 2** - The oxygen vacancies then bind to the uranium vacancy to create a bound Schottky trio:



**Step 3** - The bound Schottky trio reacts with the bubble, as in Section 3.1.3:



Recall from Section 3.1.3 that the energy of step three is equivalent to the traditional sink reaction (which is equal to the negative of the formation energy) plus a modification term to account for the bubble pressure:

$$G_{\{V_U:2V_O\}}^{bubble} = -G_{\{V_U:2V_O\}}^f + \Delta E \quad (3.25)$$

Given that kinetic barriers to steps 1 and 2 are omitted, due to high oxygen defect mobilities, they do not need to be solved for. Instead they can occur immediately upon a  $V_U$  defect encountering a sink, and the energy for steps 1, 2, and 3 can be combined to give the reaction energy for  $V_U$  with a bubble,  $G_{V_U}^{bubble}$ , as such:

$$G_{V_U}^{bubble} = -G_{\{V_U:2V_O\}}^f + G_{\{V_U:2V_O\}}^{binding} + 2G_{V_O}^f + \Delta E \quad (3.26)$$

Therefore, we simply return the traditional sink reaction energy for  $V_U$  based on the negative of the formation energy plus  $\Delta E$ :

$$V_U \xrightarrow{G_{V_U}^{bubble}} U_U + SD \quad (3.27)$$

$$G_{V_U}^{bubble} = -G_{V_U}^f + \Delta E = G_{V_U}^{sink} + \Delta E \quad (3.28)$$

Applying the same logic for  $U_i$  we obtain:

$$U_i + SD \xrightarrow{G_{U_i}^{bubble}} V_i \quad (3.29)$$

$$G_{U_i}^{bubble} = -G_{U_i}^f - \Delta E = G_{U_i}^{sink} - \Delta E \quad (3.30)$$

The modifications to the reaction energies are carried through to the driving force (see Eqs. (2.15) and (2.16)), and the new reaction rates for vacancies and interstitials interacting with a bubble are given by:

$$\frac{d[V_U]}{dt} = \begin{cases} -\frac{k_s^2}{\Omega} D_{V_U} [V_U] [sink] \left[ 1 - \exp\left(\frac{f+\Delta E}{k_B T}\right) \right], & \text{if } f + \Delta E < 0, \\ \frac{k_s^2}{\Omega} D_{V_U} [sink] \left[ \exp\left(\frac{-f-\Delta E}{k_B T}\right) - 1 \right], & \text{otherwise} \end{cases} \quad (3.31)$$

$$\frac{d[U_i]}{dt} = \begin{cases} -\frac{k_s^2}{\Omega} D_{U_i} [U_i] [sink] \left[ 1 - \exp\left(\frac{f-\Delta E}{k_B T}\right) \right], & \text{if } f - \Delta E < 0, \\ \frac{k_s^2}{\Omega} D_{U_i} [sink] \left[ \exp\left(\frac{-f+\Delta E}{k_B T}\right) - 1 \right], & \text{otherwise} \end{cases} \quad (3.32)$$

where  $f$  is the driving force for the original sink reactions, and  $\Delta E$  (Eq. (3.16)) is the modification based on  $\frac{N_{Xe}}{N_{SD}}$ .

## 3.2 Cluster dynamics simulations

### 3.2.1 Unmodified sinks

To establish a benchmark, the results of cluster dynamics simulations when using the standard sink reactions in Centipede were determined. Figures 3.5a and 3.5b show the resultant defect concentrations and diffusivities, respectively. The increase in the interstitial concentrations and the concentrations of a range of vacancy clusters towards low temperatures is clearly evident in Fig. 3.5a. These irradiation-enhanced concentrations result in an enhanced diffusion regime, as shown in Fig. 3.5b. These results have already been shown and discussed in Matthews et al. [29], however, a couple of key trends will be highlighted here. At high temperatures, the diffusivity is dominated by  $V_U$ . Between 1800 K and 1250 K, it enters the first irradiation-enhanced regime where  $\{U_i : 2O_i\}$  makes a similar contribution to  $V_U$ . Between 1250 K and 850 K,  $\{2V_U\}$  and  $\{U_i : 2O_i\}$  equally dominate diffusivity. Below 850 K, the dominant defect is  $\{U_i : 2O_i\}$ . The transition from vacancy dominated to interstitial dominated regimes as the temperature decreases is expected to be key for determining the bubble pressure.

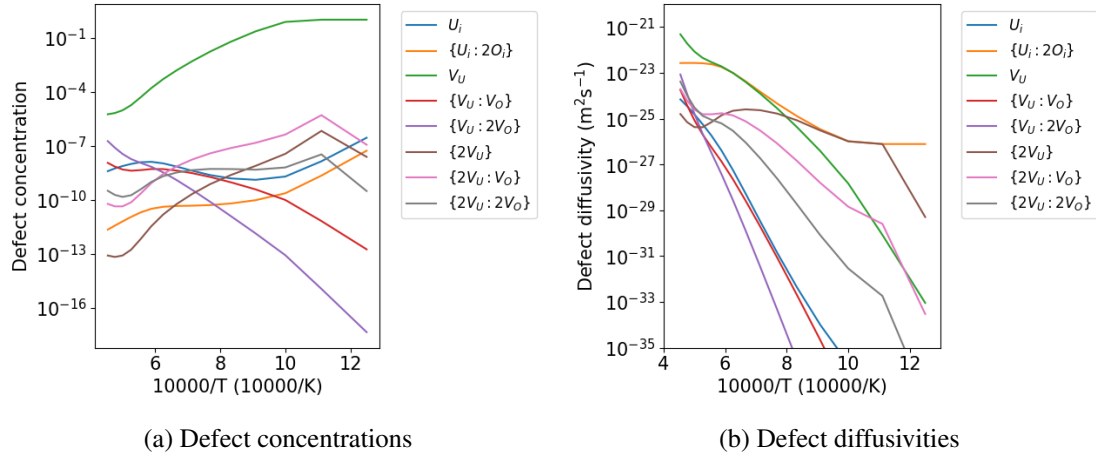


Figure 3.5: (a) The defect concentrations and (b) the defect diffusivities predicted by cluster dynamics simulations of UO<sub>2</sub> using the standard sink reactions in Centipede.

### 3.2.2 Fixed bubble pressure

Having derived modifications to the driving force that control the reaction rates for interstitials and vacancies interacting with sinks, cluster dynamics simulations can be carried out to analyze the impact that bubble pressure has on the steady-state irradiation-enhanced defect concentrations. Before coupling the bubble pressure to the defect diffusivities, first the case of constant bubble pressure is tested by varying the sink driving force and reaction rates in Centipede according to Eqs. (3.31) and (3.32), where  $\Delta E$  as a function of  $\frac{N_{Xe}}{N_{SD}}$  is given by Eq. (3.16).

Figure 3.6 shows the concentrations of  $U_i$ ,  $\{U_i : 2O_i\}$ ,  $V_U$ , and  $\{2V_U\}$  predicted as a function of  $\frac{N_{Xe}}{N_{SD}}$  for (a) 800 K and (b) 2200 K. Low and high  $\frac{N_{Xe}}{N_{SD}}$  corresponds to low and high bubble

pressures, respectively. As  $\frac{N_{Xe}}{N_{SD}} \rightarrow 0$  the modification to the sink driving forces tends to zero and the same results are obtained as for the standard Centipede simulations, as shown in Fig. 3.5. As  $\frac{N_{Xe}}{N_{SD}}$  increases, the driving force for interstitial annihilation at sinks decreases resulting in an increase in the interstitial concentrations. The increased interstitial concentration, in turn, suppresses the vacancy concentration through mutual recombination. For 800 K, the impact of bubble pressure on defect concentrations only kicks in for  $\frac{N_{Xe}}{N_{SD}} > 1.6$ , whereas at 2200 K much lower bubble pressures can influence the defect concentrations. This is due to the fact that at high temperatures the defects are much closer to their thermal equilibrium concentrations, and are, therefore, sensitive to subtle changes in the sink driving force. Conversely, at low temperatures the defects are at high concentrations, so the bracketed terms in Eqs. (3.31) and (3.32) are equal to 1, until  $f \rightarrow 0$  for the interstitial reaction at high bubble pressures, at which point the sink rate goes to zero and the interstitial concentrations increase. This causes a corresponding decrease in the vacancy concentrations due to higher mutual recombination rates, whereby higher concentrations of mobile interstitials recombine with the immobile vacancies. One outcome from this is the reduction in the  $V_U$  concentration to more realistic concentrations in the low temperatures regime.

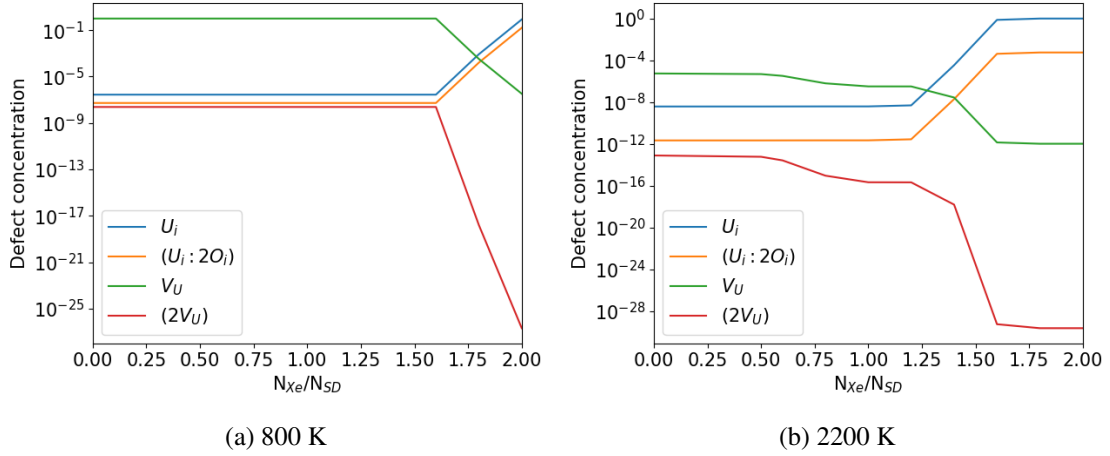


Figure 3.6: The defect concentrations predicted by cluster dynamics simulations of  $\text{UO}_2$ , where the sink reactions in Centipede have been modified for different constant bubble pressures according to Eqs. (3.31) and (3.32). The simulations were run at (a) 800 K and (b) 2200 K. (a) and (b) show a subset of the defects considered by Centipede.

### 3.2.3 Variable bubble pressure

Now that the modifications to defect-bubble sink reactions have been shown influence the defect concentrations for high bubble pressures and follow trends that are intuitive, the rate of those reactions must be used to update the bubble pressure. The interaction of interstitials or vacancies with a bubble changes the concentration of SDs, the species used to describe the  $\text{UO}_2$  formula units removed to create the voids that make up the bubbles. Therefore, the rate of change of

[SD] is given by:

$$\frac{d[SD]}{dt} = \frac{d[U_i]}{dt} - \frac{d[V_U]}{dt} \quad (3.33)$$

where  $\frac{d[U_i]}{dt}$  and  $\frac{d[V_U]}{dt}$  are given by Eqs. (3.31) and (3.32). However, we wish to solve for the rate of change of the bubble pressure, as represented by  $\frac{N_{Xe}}{N_{SD}}$ . Instead of solving directly for  $\frac{N_{Xe}}{N_{SD}}$  we solve for  $\frac{N_{SD}}{N_{Xe}}$ , so that its rate equation can be expressed in terms of the interstitial and vacancy sink rates:

$$\frac{d\left(\frac{N_{SD}}{N_{Xe}}\right)}{dt} = \frac{1}{[Xe]} \frac{d[U_i]}{dt} - \frac{1}{[Xe]} \frac{d[V_U]}{dt} \quad (3.34)$$

where  $[Xe]$  is the concentration of Xe contained within the bubbles averaged over the fuel volume. The physics to simulate the flux of Xe arriving or being resolved through damage events has not been included yet, so  $[Xe]$  is constant. On this basis, a new solved variable  $SD\_Xe$  has been define in Centipede representing  $\frac{N_{SD}}{N_{Xe}}$ .

As a preliminary step, the concentration of Xe in bubbles,  $[Xe]$ , has been roughly estimated as 0.0085 based on a fission gas yield of 20% per fission event, a burnup of 8.5%, and assuming roughly half of the Xe atoms remain in bubbles. At this stage we have also not tried to distinguish between intra- and inter-granular bubbles but will do so in future work. This initial bubble pressure was set to  $\frac{N_{Xe}}{N_{SD}} = 0.5$  ( $\frac{N_{SD}}{N_{Xe}} = 2$ ).

Figures 3.7a and 3.7b show the defect concentrations predicted by also solving for bubble pressure and Figure 3.7c shows the steady-state bubble pressure. There are three regimes of behavior that can be seen:

1. Above 1800 K, as was also the case using the standard sinks, the defect concentrations remain at the initial conditions of thermal equilibrium and  $\frac{N_{Xe}}{N_{SD}} = 0.5$ . Figure 3.4 shows that for  $\frac{N_{Xe}}{N_{SD}} = 0.5$  there is a negligible change from the standard sink driving force, so the results are unchanged with respect to Figures 3.5a and 3.5b.
2. From 1800 K to 1250 K, the  $V_U$  and  $\{U_i : 2O_i\}$  contributions to diffusivity are similar. At this point the bubble pressure begins to increase. However, given the similar arrival rates from vacancies and interstitials at the bubble,  $\frac{N_{Xe}}{N_{SD}}$  reaches steady state only a little higher than the initial conditions.
3. Below 1250 K,  $V_U$  diffusivity drops significantly below that of  $\{U_i : 2O_i\}$ , due to the lower mobility of  $V_U$ . Therefore, there is a much greater rate of arrival at bubbles for  $\{U_i : 2O_i\}$  compared to  $V_U$ , which pushes up the bubble pressure dramatically. It converges on a solution where the rate of arrival of interstitials eventually tends to zero as the high bubble pressure pushes the driving force to zero. This further increases the interstitial concentration, which, in turn, suppresses the vacancy concentration through mutual recombination. As a result, for low temperatures, the new model tends to high bubbles pressures, and has higher interstitial concentrations and lower vacancy concentrations compared to the original model.

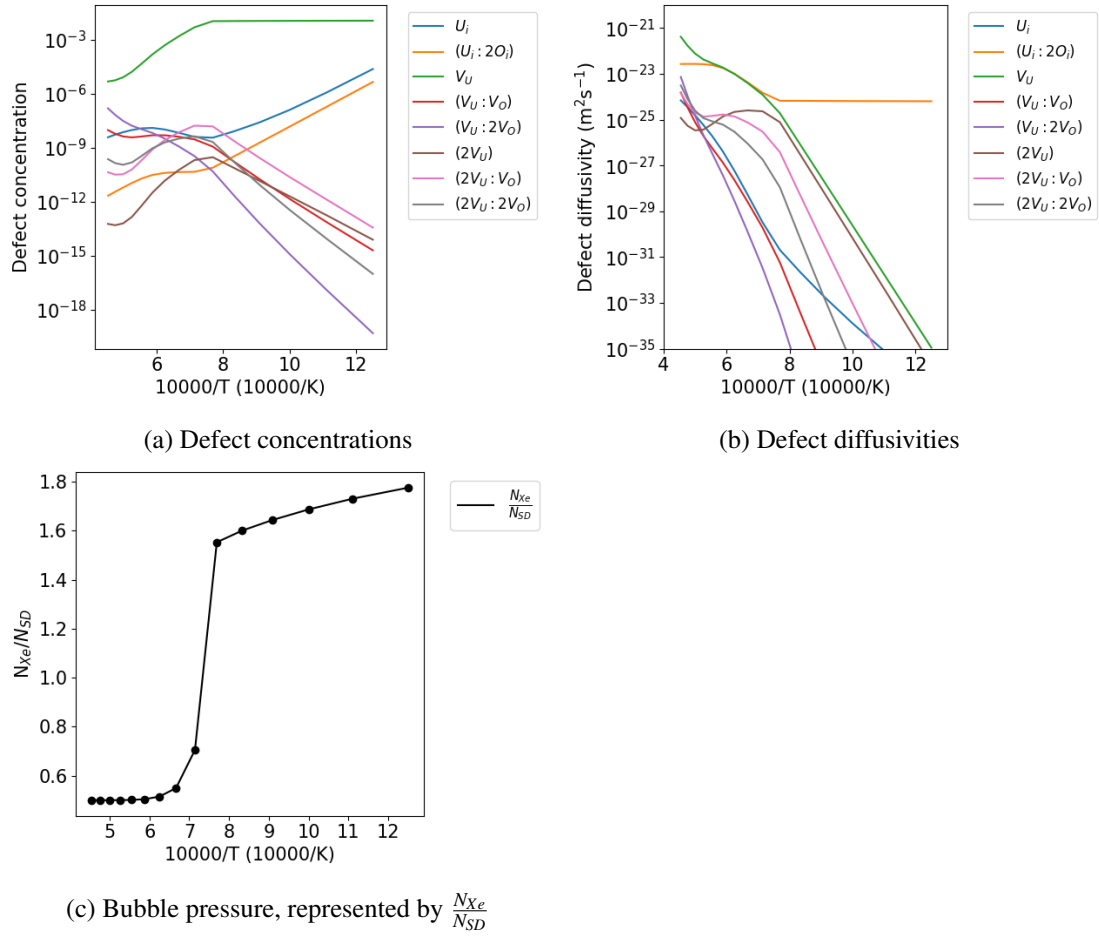


Figure 3.7: (a) The defect concentrations and (b) the defect diffusivities predicted by cluster dynamics simulations of  $UO_2$ , where (c) the steady-state bubble pressure is also solved for.

Although we have not explicitly transformed this into a bubble pressure (i.e. in units of Pa), Fig. 3.7c represents a very significant increase in pressure at the low temperatures relevant to the periphery of the pellet where HBS forms. Therefore, it is expected that bubbles present in HBS will become highly over-pressurized during steady-state reactor operation. These high pressure bubbles, that form a solid Xe lattice at low T (relevant to the periphery of the pellet under normal operating conditions), will expand rapidly during a temperature ramp, possibly going through solid-liquid and liquid-gas phase transitions. The pressure expected to be exerted on the  $UO_2$  matrix during that process, means these bubbles are a likely precursor to the fragmentation of high burnup fuel during a temperature ramp.

The final steady-state results were found to be sensitive to the initial conditions, as shown for the bubble pressure in Fig. 3.8. Using lower values of  $\frac{N_{Xe}}{N_{SD}}$  resulted in a decrease in the temperature for the transition between low and high pressure bubbles. Conversely, a higher initial value of  $\frac{N_{Xe}}{N_{SD}}$  increased the transition temperature. Above the transition temperature,  $\frac{N_{Xe}}{N_{SD}}$

remained at the initial value, while below the transition temperature,  $\frac{N_{Xe}}{N_{SD}}$  converges to a similar value regardless of the initial conditions. Although future work should investigate this sensitivity to the initial conditions and determine the most appropriate initial choice of  $\frac{N_{Xe}}{N_{SD}}$ , this will not change the key result, in the context of fragmentation, that the low temperature bubbles are highly over-pressurized.

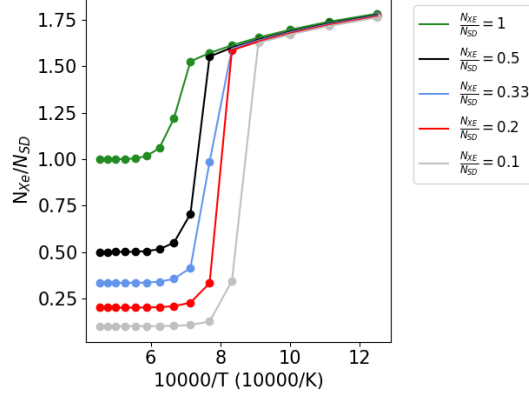


Figure 3.8: The steady-state bubble pressure, represented by  $\frac{N_{Xe}}{N_{SD}}$ , determined using different initial values of  $\frac{N_{Xe}}{N_{SD}}$ .

Future work will apply a similar approach to investigate the impact of including bubble pressure in the cluster dynamics framework for Xe diffusion from Matthews et al. [30]. We will also investigate the role of other sinks, such as dislocations or grain boundaries, on the bubble pressure. Eventually this should be spatially resolved in a microstructure-aware code to fully capture the effects of various sinks in high burnup structure. By capturing the evolution of these sinks during irradiation, the bubble pressures can, thus, be predicted as a function of burnup. Only zero K MD bubble data has been used, which prevents pressure-release mechanisms, such as dislocation loop punching, that may occur at finite temperature. MD simulations should be used in future work to test for this possibility for high pressure bubbles. Additionally, by carrying out MD simulations of the high pressure bubbles at grain boundaries during temperatures ramps, we can assess the likelihood that such bubbles cause fragmentation (currently being investigated under an EPRI project). Having a threshold for fragmentation based on a fundamental understanding of the evolution of bubble pressure as a function of burnup will enable the development of more mechanistic fragmentation thresholds in BISON.

## 4 Conclusions

Fragmentation of high burnup fuel is a significant safety concern due to the relocation of the fuel fragments within the fuel pin, which causes a redistribution of power. High pressure bubbles in HBS, which forms in the low temperature periphery of  $\text{UO}_2$  pellets, are thought to contribute fragmentation. In this work, we explore a cluster dynamics approach to predicting bubble pressure as a function of temperature under irradiation conditions.

MD simulations have been carried out on bubbles of various sizes and pressures to derive an expression for the reaction energies for U interstitials and vacancies interacting with a bubble. It was shown that the reaction energy for a vacancy becomes progressively more exothermic for high bubble pressures, due to the release of energy from the gas as its pressure is relieved. Conversely, the annihilation of an interstitial at a bubble compresses the gas, such that the reaction energy becomes less exothermic for high bubble pressures. At sufficiently high pressures the interstitial reaction becomes endothermic. It was shown that the pressure-dependent reaction energies were broadly independent of bubble size and could be expressed as a function of the ratio of Xe atoms to SD units that make up the bubble, where SD is a  $\text{UO}_2$  formula unit removed from the lattice to form the void. The bubbles are made up of  $N_{SD}$  SD units and  $N_{Xe}$  Xe atoms.

The MD-derived reaction energies as a function of  $\frac{N_{Xe}}{N_{SD}}$  were reformulated as a modification to the sink reactions for U interstitials and vacancies in the cluster dynamics code Centipede. This code has been shown previously to accurately capture the diffusion of point defects and clusters in  $\text{UO}_2$ . The bubble pressure was added as a solved variable to Centipede to enable the steady-state bubble pressure to be determined. We found that there is a transition from low pressure bubbles, at high temperature, to high pressure bubbles, at low temperature. This supports the hypothesis that bubbles become over-pressurized in the periphery of the fuel pellet, where HBS forms, due to irradiation-enhanced interstitial diffusion. Future work will examine the impact of bubble pressures on Xe diffusion and the influence of others sinks (e.g. dislocations and grain boundaries relevant to HBS) on bubble pressure.



## **Acknowledgments**

This work was funded by the US Department of Energy, Office of Nuclear Energy, Nuclear Energy Advanced Modeling and Simulation (NEAMS) program. Los Alamos National Laboratory, an affirmative action/equal opportunity employer, is operated by Triad National Security LLC, for the National Nuclear Security Administration of the U.S. Department of Energy under Contract No. 89233218CNA000001.

## References

- [1] V. V. Rondinella and T. Wiss. *Materials Today*, 13:24–32, 2010.
- [2] K. Nogita and K. Une. *Journal of Nuclear Materials*, 226:302–310, 1995.
- [3] K. Nogita and K. Une. *Nucl. Instr. Meth. Phys. Res. B.*, 91:301–306, 1994.
- [4] K. Une, K. Nogita, S. Kashibe, and M. Imamura. *Journal of Nuclear Materials*, 188:65–72, 1992.
- [5] T. Sonoda, M. Kinoshita, I. L. F. Ray, T. Wiss, H. Thiele, D. Pellottiero, V. V. Rondinella, and Hj. Matzke. *Nucl. Instr. Meth. Phys. Res. B.*, 191:622–628, 2002.
- [6] T. Wiss, H. Thiele, A. Janssen, D. Papaioannou, V. V. Rondinella, and R. J. M. Konings. *Journal of Materials*, 64:6–9, 2012.
- [7] M. Kinoshita, T. Kameyama, S. Kitajima, and Hj. Matzke. *Journal of Nuclear Materials*, 252:71–78, 1998.
- [8] N. Lozano and L. Desgranges. *Journal of Nuclear Materials*, 257:78–87, 1998.
- [9] I. L. F. Ray, Hj. Matzke, H. Thiele, and M. Kinoshita. *Journal of Nuclear Materials*, 245:115–123, 1997.
- [10] C. T. Walker, D. Staicu, M. Sheindlin, D. Papaioannou, W. Goll, and F. Sontheimer. *Journal of Nuclear Materials*, 350:19–39, 2006.
- [11] C. T. Walker. *Journal of Analytical Atomic Spectrometry*, 14:447–454, 1999.
- [12] X-M. Bai, M. R. Tonks, Y. Zhang, and J. D. Hales. *Journal of Nuclear Materials*, 470:208–215, 2016.
- [13] J. A. Turnbull, S. K. Yagnik, M. Hirai, D. M. Staicu, and C. T. Walkert. *Nuclear Science and Engineering*, 179:477–485, 2015.
- [14] R. A. Jackson and C. R. A. Catlow. *Journal of Nuclear Materials*, 127:167–169, 1985.
- [15] X. Y. Liu, B. P. Uberuaga, D. A. Andersson, C. R. Stanek, and K. E. Sickafus. *Applied Physics Letters*, 98:151902, 2011.
- [16] A. Thompson and C. Wolverton. *Physical Review B*, 84:1–11, oct 2011.

- [17] D. A. Andersson, P. Garcia, X.-Y. Liu, G. Pastore, M. Tonks, P. Millett, B. Dorado, D. R. Gaston, D. Andrs, R. L. Williamson, R. C. Martineau, B. P. Uberuaga, and C. R. Stanek. *Journal of Nuclear Materials*, 451:225–242, aug 2014.
- [18] D. A. Andersson, M. R. Tonks, L. Casillas, S. Vyas, P. Nerikar, B. P. Uberuaga, and C. R. Stanek. *Journal of Nuclear Materials*, 462:15–25, 2015.
- [19] E. Vathonne, D. A. Andersson, M. Freyss, R. Perriot, M. W.D. Cooper, C. R. Stanek, and M. Bertolus. *Inorganic Chemistry*, 56:125–137, 2017.
- [20] D. A. Andersson, B. P. Uberuaga, P. V. Nerikar, C. Unal, and C. R. Stanek. *Physical Review B - Condensed Matter and Materials Physics*, 84:1–12, 2011.
- [21] R. Perriot, C. Matthews, M. W D Cooper, B. P Uberuaga, Christopher R Stanek, and David A Andersson. *Journal of Nuclear Materials*, 520:96–109, 2019.
- [22] C. R. A. Catlow. *Radiation Effects*, 53:127–132, 1980.
- [23] X-Y. Liu and D. A. Andersson. *Journal of Nuclear Materials*, 462:8–14, 2015.
- [24] S. T. Murphy, A. Chartier, L. Van Brutzel, and J. P. Crocombette. *Physical Review B - Condensed Matter and Materials Physics*, 85:1–9, 2012.
- [25] M. Huang, D. Schwen, and R. S. Averbach. *Journal of Nuclear Materials*, 399:175–180, 2010.
- [26] K. Govers, C. L. Bishop, D. C. Parfitt, S. E. Lemehov, M. Verwerft, and R. W. Grimes. *Journal of Nuclear Materials*, 420:282–290, jan 2012.
- [27] W. Setyawan, M. W.D. Cooper, K. J. Roche, R. J. Kurtz, B. P. Uberuaga, D. A. Andersson, and B. D. Wirth. *Journal of Applied Physics*, 124, 2018.
- [28] S. T Murphy, P. C. M Fossati, and R. W. Grimes. *Journal of Nuclear Materials*, 466:634–637, 2015.
- [29] C. Matthews, R. Perriot, M. W D Cooper, C. R. Stanek, and D. A Andersson. *Journal of Nuclear Materials*, 527:151787, 2019.
- [30] C. Matthews, R. Perriot, M. W. D. Cooper, C. R. Stanek, and D. A. Andersson. *Journal of Nuclear Materials*, 540:152326, 2020.
- [31] M. W. D. Cooper, M. J. D. Rushton, and R. W. Grimes. *Journal of Physics: Condensed Matter*, 26:105401, mar 2014.
- [32] S. Plimpton. *Journal of Computational Physics*, 117:1–19, 1995.
- [33] M. S. Daw and M. I. Baskes. *Phys. Rev. B*, 29:6443–6453, 1984.
- [34] P. P. Ewald. *Ann. Phys.*, 64:253, 1921.

- [35] R. W. Hockney and J. W. Eastwood. *Computer Simulation Using Particles*. McGraw-Hill, New York, 1988.
- [36] P. M. Morse. *Phys. Rev.*, 34:57–64, 1929.
- [37] R. A. Buckingham. *Proceedings of the Royal Society of London. Series A, Mathematical and Physical Sciences (1934-1990)*, 168:264–283, 1938.
- [38] M. W. D. Cooper, N. Kuganathan, P. A. Burr, M. J.D. Rushton, R. W. Grimes, C. R. Stanek, and D. A. Andersson. *Journal of Physics Condensed Matter*, 28:405401, 2016.
- [39] K. T. Tang and J. P. Toennies. *Journal of Chemical Physics*, 118:4976–4983, 2003.
- [40] F. A. Kröger and H. J. Vink. *J. Solid State Phys.*, 3:307–435, 1956.
- [41] R. J. White and M. O. Tucker. *Journal of Nuclear Materials*, 118:1–38, 1983.
- [42] C Baker. *Journal of Nuclear Materials*, 66:283–291, 1977.